THE JOURNAL OF PHYSICAL CHEMISTRY C

pubs.acs.org/JPCC Article

Fracture Toughness and Surface Energy Density of Kerogen by Molecular Dynamics Simulations in Tensile Failure

Tianhao Wu and Abbas Firoozabadi*

Cite This: J. Phys. Chem. C 2020, 124, 15895−15901 Read Online

ACCESS | Metrics & More | Article Recommendations | Supporting Information

ABSTRACT: Fracture toughness and surface energy density are critical parameters in the simulation of hydraulic fracturing in shale formations. In this study, a microscopic insight into the mechanisms of tensile failure in kerogen is advanced by molecular dynamics simulations for the first time. The elastic properties, critical stress, surface energy density, and fracture toughness of kerogen are analyzed systematically. Our work reveals that kerogen is potentially a weak component in shale, which may serve as a region of fracture initiation and preferential fracture propagation path. The critical energy release rate G_c is higher than the doubled surface energy density γ_s ($G_c \geq 2\gamma_s$), which indicates that there may be pronounced plastic deformation in kerogen in the tensile failure. This work sets the stage for the determination of various shale mechanical properties and surface energy density to examine fracturing effectiveness in shale media from the molecular scale.

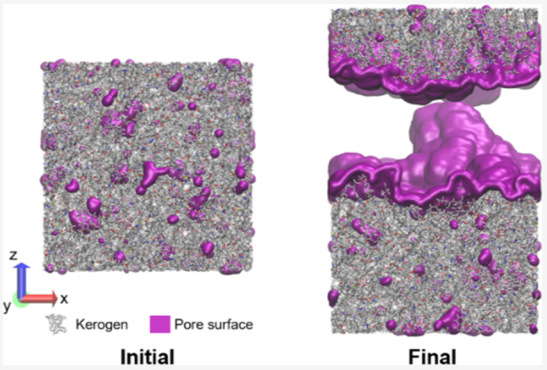

1. INTRODUCTION

Hydrocarbon production from organic-rich shale formations has changed the worldwide energy outlook.[1,2] Commercial development of shale oil and gas formations relies on multistage fracturing. Water is the dominant fracturing fluid because of its low cost and wide availability.[3] However, hydraulic fracturing by water requires an enormous amount of this fluid and poses a potential threat to the environment because of a large amount of flow-back wastewater from wells containing toxic chemical additives.[4] Nonaqueous fracturing fluids have been proposed to improve the fracturing process in shale formations and to advance environmental stewardship. CO_2 is considered to be one of the most promising fracturing fluids because of its various merits, including a higher fracture density, lower fracturing pressure, and less sensitivity to reservoir rock species.[5−7] The mechanism of fracturing by CO_2 is largely unknown. In this regard, molecular simulations are proposed as a powerful tool to advance the understanding of the microscopic mechanisms in shale fracturing. The methodology should be established first.

Tensile failure is the key process in hydraulic fracturing.[8] Fracture toughness is defined to be a measure of the ability of a material to resist fracture propagation. It is often characterized by the critical energy release rate G_c, which is defined as the critical value of the stored strain energy released per unit crack area at the moment of fracture extension in elastic materials.[9,10] The term "rate" does not refer to a derivative with respect to "time" but to the rate of change in energy with the crack area. Griffith[11,12] established the theory of brittle failure based on the surface energy density γ_s as $G_c = 2\gamma_s$. Irwin[10,13,14] extended Griffith's concept by taking into account the energy required to create a damaged zone of plastic deformation ahead of the crack tip. Irwin's work proposes that $G_c = 2(\gamma_s + \gamma_p)$, where γ_p is the plastic work per unit area of the surface created.[9] By assuming that the strain energy is fully released after rupture, the strain energy is equal to the total work that has been done for creating the new crack area. G_c can be obtained by integrating the stress−strain curve based on the equation[15−17]

$$G_c = \frac{1}{A_{crack}} \int_{loading} F dl = \frac{V}{A_{crack}} \int_{loading} \sigma d\varepsilon \quad (1)$$

where V is the initial volume of the system, F is the external force, l is the sample length along the direction of tension, and σ and ε are the stress and strain in the z-direction, respectively. A_{crack} is the total crack area created by tensile failure.[15−17] The critical stress intensity factor K_{Ic} is another important measure of fracture toughness for the stress intensity approach.[9] It is related to G_c as[9]

$$K_{Ic} = \sqrt{G_c E'} = \sqrt{G_c \frac{E}{(1-\nu^2)}} \quad (2)$$

Received: April 8, 2020
Revised: June 24, 2020
Published: June 24, 2020

https://dx.doi.org/10.1021/acs.jpcc.0c03158
J. Phys. Chem. C 2020, 124, 15895−15901

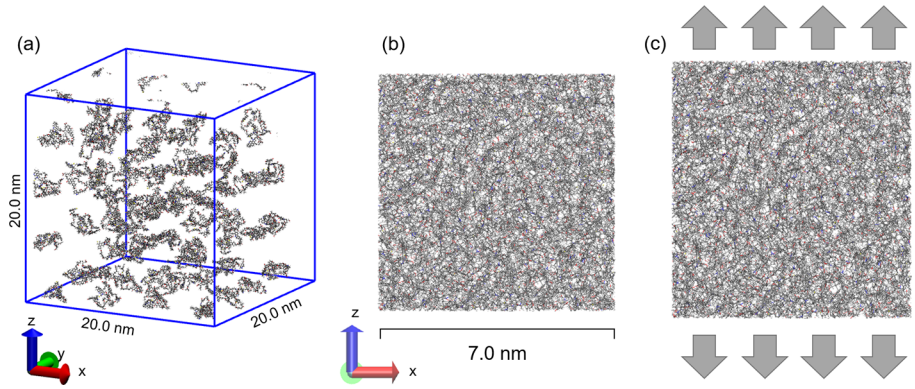

Figure 1. Sketch of kerogen matrix construction and extension process. (a) Initial configuration of type-II kerogen macromolecules (60 units); (b) kerogen matrix; and (c) sketch of extension in the kerogen matrix.

where E' is the elastic modulus under plane strain, E is Young's modulus, and ν is Poisson's ratio.

Fracture toughness is a crucial parameter in the numerical simulations of hydraulic fracturing.[18,19] For example, G_c is a key parameter in the phase-field method for simulating fracture propagation. Generally, the studies are limited to homogeneous media despite the fact that shale has significant heterogeneity at the microscale.[20] The significant difference in the properties of organic and inorganic matter may have a large effect on the overall mechanical properties of the shale rock. To gain insights at the microscale, molecular dynamics (MD) simulations of tensile failure are performed on typical minerals. Patil et al.[21] have performed a comparative study of MD simulations and phase-field simulations of tensile failure in aragonite, which is brittle. Their results confirm that the parameters from MD simulations can be used in the continuum approach, such as the phase-field method, and capture the tensile failure process. Hantal et al.[15] and Brochard et al.[16] have carried out molecular simulations to determine the mechanical properties and tensile failure of illite, silica, and porous carbon. The pre-existing fractures are also included to study the toughness and the relationship between the fracture length and critical stress. In a recent study, a composite material consisting of clay−porous carbon was created to investigate the mechanical properties and failure modes.[17,22] The authors show that the results are significantly affected by the interfacial bond density and heterogeneity.

Kerogen is an important component of most organic-rich shale rocks. Its mechanical properties are distinctly different from minerals and porous carbon. It is usually classified based on maturity indicators, including the vitrinite reflectance, aromatic-to-aliphatic ratio, and hydrogen-to-carbon (H/C) and oxygen-to-carbon (O/C) atomic ratios. Various representative structures of kerogens have been constructed based on the geochemical properties from experiments.[23,24] Bousige et al.[23] studied the tensile failure process due to bond breaking. Wu and Firoozabadi[25] studied the tensile and shear failure in different types of kerogen and provided the link to macroscopic simulations through the failure envelope. However, the understanding of tensile failure mode is at an early stage. The fracture toughness and surface energy density of kerogen have not yet been reported from simulations and measurements to the best of our knowledge.

In this investigation, molecular simulations of tensile failure in realistic kerogen matrices are performed. We demonstrate the methodology based on the type II-A kerogen matrix. The effects of kerogen type and maturity on tensile failure and the relationship between fracture toughness and surface energy density are investigated systematically.

2. METHODS

We apply MD simulations using a large-scale atomic/molecular massively parallel simulator (LAMMPS) in this study.[26] The molecular structures are rendered using visual molecular dynamics (VMD).[27] The kerogen macromolecule units are constructed based on the molecular structures from Ungerer et al.,[24] which reproduce the elemental and functional data of kerogen including the H/C, O/C, and N/C ratios, the average aromaticity, and the average size of the aromatic unit (Figure S1). We use the type II-A kerogen to demonstrate the methodology.

To investigate the tensile failure, we create a kerogen matrix of much larger size than that employed in the studies for adsorption and diffusion.[28−32] We place 60 kerogen macromolecules at random positions in a cubic box with a side length of 20.0 nm (Figure 1a). The periodic boundary condition is applied to all three directions. The all-atom model is constructed with the polymer consistent force field plus (PCFF+) by using MedeA.[24,33,34] A cutoff of 14 Å is set for the short-range interactions. The long-range interactions are computed using the PPPM method with an accuracy of 1×10^{-5}.[35] The Waldman−Hagler combining rules are used for the Lennard-Jones (LJ) interactions.[36] In the first step, we perform an annealing process with a series of barostat and Nose−Hoover thermostat (Table S1). The temperature for the annealing step ranges from 300 to 1000 K. The final temperature is 298.15 K, which is also the temperature for all of the calculations in the following sections. Finally, we construct a kerogen matrix with a size of $7.0 \times 7.0 \times 7.0$ nm^3 (Figure 1b). Because of the different depositional environments and geological processes, the kerogens possess various molecular structures, which may result in different mechanical properties. The anisotropy of the matrix due to the geological process of sedimentation is not taken into account, which is relatively weak at the nanoscale.[7,20] To investigate the effect of kerogen type and maturity on mechanical properties, we construct different kerogen matrices with a similar size consisting of the representative macromolecules in Figure S1. By using the same method, we construct the kerogen matrices of types I-A, III-A, II-B, II-C, and II-D with 60, 75, 70, 70, and 120 macromolecules, respectively (see Figure S2). The radial distribution function between carbon atoms is provided in

https://dx.doi.org/10.1021/acs.jpcc.0c03158
J. Phys. Chem. C 2020, 124, 15895−15901

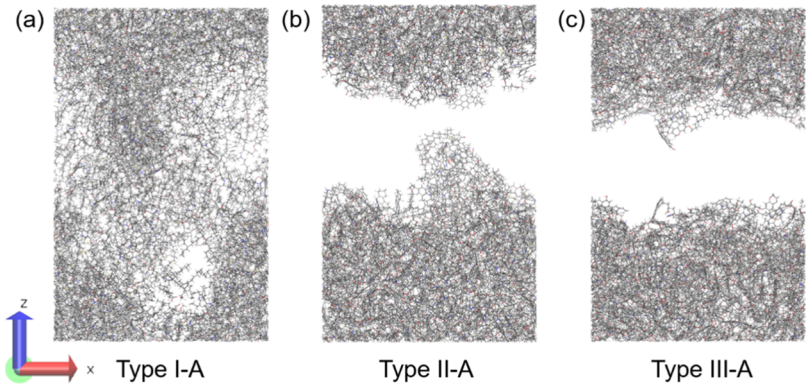

Figure 2. Tensile failure modes of different kerogen types. Type I-A kerogen has fully ductile behavior. Type III-A kerogen shows an abrupt breakdown and a relatively flat fracture surface, which reveal moderate brittle behavior. Type II-A kerogen has milder brittleness.

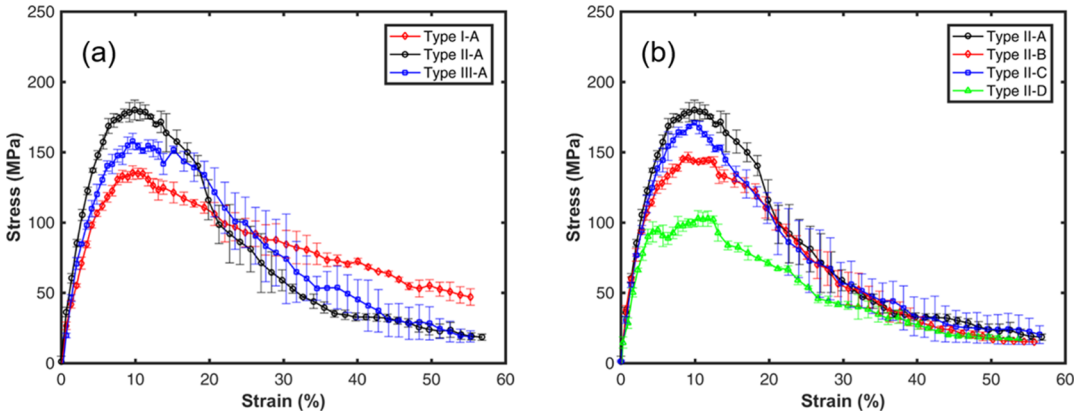

Figure 3. Tensile stress−strain relationship of different types of kerogens. The error bars are from three simulations with different initial conditions. The tensile stress and strain are defined as positive. The extension is performed under plane-strain in which the dimensions in the plane perpendicular to the direction of tension are kept constant.

Figure S3, which agrees with Ungerer et al.[24] The porosity of the constructed kerogen matrices has a significant difference because of distinctly different molecular structures. The porosity ranges from 0.6 to 9.0%, which is due to the molecular structure of kerogen macromolecules. Kerogens of types III-A and II-D have much higher porosity and a relatively larger pore size than the others, while type I-A kerogen has the lowest porosity where one can barely find large pores. As for type II kerogen matrices, the porosity of the constructed matrix increases with the increase of maturity. The pore size distribution is presented in Figure S4.

We perform a quasistatic strain-driven mechanical process to simulate the tensile failure and obtain the mechanical properties.[15−17] A series of small tensile plane strains are applied in the z-direction, in which the strains perpendicular to the extension are prevented.[12,15−17] The displacements of each stage are set to 0.5 Å in the first 20 stages and 1.0 Å for the later stages, respectively. At each stage, the temperature is maintained by using the Nose−Hoover thermostat at 298.15 K. The simulation time of each stage is 200 ps with a time step of 1 fs, and the data of the last 100 ps are statistically averaged to determine the properties. The simulations are repeated three times to obtain the error bar. We have examined that there is no size dependency on the mechanical properties at this scale (see the Supporting Information, Figures S5−S8).

3. RESULTS AND DISCUSSION

3.1. Tensile Failure. The three types of immature kerogen matrices (I-A, II-A, and III-A) exhibit significantly different failure modes. The tensile failure process is shown in Figure S9 with a series of snapshots at various strains, and the final structures at ε ∼55% are presented in Figure 2. Type I-A kerogen has fully ductile behavior. The molecules are entangled even at strain as high as 55%. However, type III-A kerogen shows an abrupt breakdown and a relatively flat fracture surface, which reveals moderate brittle behavior. Type II-A kerogen shows milder brittleness. The tensile stress−strain relationships are presented in Figure 3a. All three matrices show an elastic region, followed by a plastic region before rupture. Type II-A and type III-A kerogens have a clear abrupt breakdown, while type I-A kerogen shows a continuous decrease of stress after rupture. These behaviors are also confirmed through the phenomena demonstrated in Figure S9. The failure mechanism is significantly affected by the kerogen type. The kerogen with a higher content of aliphatic carbons reveals a more ductile behavior and lower porosity, while a higher content of aromatic carbons may result in pronounced brittleness and high porosity. The critical stress σ_c is defined as the maximal stress before rupture. Type II-A kerogen has the highest critical stress, followed by type III-A and then type I-A. As for the type II kerogen with different maturities, the matrices reveal a similar behavior except for type II-D (see Figure 3b). Types II-A, II-B, and II-C kerogens have critical

https://dx.doi.org/10.1021/acs.jpcc.0c03158
J. Phys. Chem. C 2020, 124, 15895−15901

stresses of 146−180 MPa, followed by a clear breakdown. The breakdown in type II-D is not pronounced, which is mainly due to the low critical stress.

To understand the elementary processes of plasticity, we perform a detailed analysis based on type II-A kerogen. The radial distribution function between carbon atoms and the pore size distribution at the initial condition (ε = 0%), at the yield point (ε = 4.97%), and around critical stress (ε = 10.65%), are calculated. The results indicate that there is no appreciable change in radial distribution function between carbon atoms under different strains (see Figure S10), which implies that the plasticity process is not dominated by intramolecular interactions. Based on pore size distributions (see Figure 4), the creation and growth of void space in the

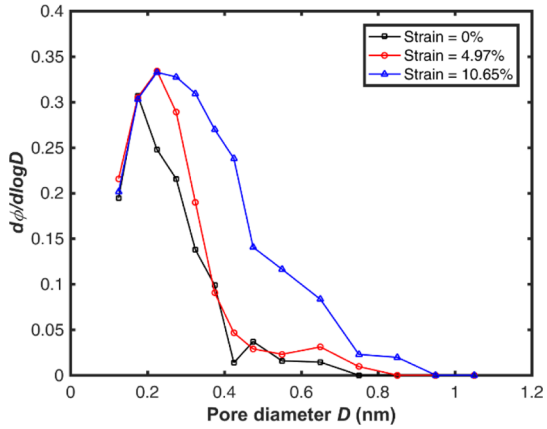

Figure 4. Evolution of pore size distribution in type II-A kerogen matrix. The yield point is around ε = 4.97%, followed by a plastic region. The critical stress appears around ε = 10.65%.

elastic region (ε < 4.97%) are in the range of 0.2−0.4 nm, which are mainly in isolated pores. In the plastic region (ε = 4.97−10.65%), the pore space below 0.25 nm reaches a balance, and a large number of pores above 0.25 nm appear. According to the evolution of pore space distribution from ε = 4.97 to 10.65% (see Figure S11), most of the pores grow independently, and a relatively small amount of space is generated by pore coalescence. These behaviors are in line with the typical fracture evolution in the ductile material.[9]

Kerogens generally have experienced decomposition processes during the geological time (million-year scale), which may lead to heterogeneity. The representative molecules used in this study are constructed based on geochemical data regardless of different cross-linking degrees. Intermolecular interactions dominate the failure process based on these representative molecules. The results mainly represent the lower limit of critical stress. Cross-linking may strengthen the material. An extreme condition is that all the molecules are highly cross-linked as one giant molecule, which can lead to higher critical stress controlled by bond breaking. However, the fracture initiation and propagation may be mainly dominated by the weakest component in heterogeneous media, especially in the highly decomposed region.

3.2. Elastic Properties, Surface Energy Density, and Fracture Toughness. Young's modulus and Poisson's ratio are calculated based on the data with strain ε <2.5% (see Table 1). The methods are provided in the Supporting Information. Young's modulus of the kerogen matrix ranges from 1.6 to 3.2 GPa, which is in the same range as the values of compression (1.5−3.6 GPa).[25] It is also in the same order of magnitude as the experimental data based on nanoindentation, modulus mapping, and atomic force microscopy from the literature (3.2−29.1 GPa).[37−40] The deviation may be due to the difference in the scale between the MD simulations and experiments. Poisson's ratio of kerogen ranges from 0.36 to 0.59, which is much higher than the other minerals in shale, including quartz (~0.08), illite (0.285−0.315), and carbonate (0.29−0.31).[41,42] The results of types I-A, II-A, and III-A agree with the results based on compression (0.24−0.42).[25]

To calculate G_c, we perform the integration of the stress−strain curve for the whole range. The created surface area is defined as the difference in the surface area of the initial and final conditions. The surface area is calculated by taking helium as the probe molecule.[43,44] An example in type II-A kerogen is presented in Figure 5. The crack area A_{crack} is different from the

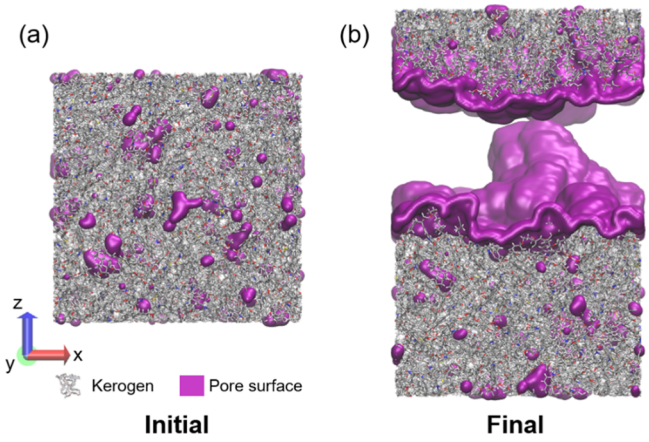

Figure 5. Pore surface of type II-A kerogen matrix made of 60 units of macromolecules. (a) Initial surface area = 27 m^2/g (ε = 0%) and (b) final surface area = 303 m^2/g after rupture (ε = 57%). Periodic boundary conditions are applied in all three directions. The outside surface of the domain is excluded. The total created surface area is 276 m^2/g (=303−27 m^2/g). The crack area A_{crack} is defined as half of the created surface area (138 m^2/g).

Table 1. Young's Modulus E, Poisson's Ratio ν, Critical Stress σ_c, Surface Energy Density γ_s, Critical Energy Release Rate G_c, and Critical Stress Intensity Factor K_{Ic} of the Kerogen Matrix in Different Organic Types and Maturities

kerogen	E (GPa)	ν	σ_c (MPa)	γ_s (J/m^2)	G_c (J/m^2)	K_{Ic} (MPa·m$^{1/2}$)
type I-A	1.6 ± 0.2	0.48 ± 0.02	135 ± 2	0.089 ± 0.008	0.282 ± 0.007	0.024 ± 0.001
type II-A	2.7 ± 0.3	0.45 ± 0.01	180 ± 5	0.107 ± 0.010	0.298 ± 0.027	0.032 ± 0.002
type III-A	3.2 ± 0.2	0.36 ± 0.02	158 ± 2	0.104 ± 0.010	0.283 ± 0.017	0.032 ± 0.001
type II-B	2.4 ± 0.5	0.45 ± 0.02	146 ± 2	0.095 ± 0.010	0.247 ± 0.004	0.026 ± 0.002
type II-C	2.6 ± 0.2	0.34 ± 0.01	171 ± 1	0.118 ± 0.011	0.279 ± 0.001	0.030 ± 0.001
type II-D	1.7 ± 0.1	0.59 ± 0.04	103 ± 3	0.107 ± 0.011	0.256 ± 0.016	0.026 ± 0.001

https://dx.doi.org/10.1021/acs.jpcc.0c03158
J. Phys. Chem. C 2020, 124, 15895−15901

surface area. The crack area is defined as the projected area of the fracture, which often refers to the cross-sectional area of the domain or the created crack length multiplied by the thickness of the sample.[9,17] In this study, we define A_{crack} as half of the total created surface area. To examine the theories of Griffith and Irwin, we also calculate the surface energy density of kerogen matrices. The method is provided in the Supporting Information.

The G_c and K_{Ic} of kerogen are about 0.3 J/m^2 and 0.03 MPa·m$^{1/2}$, respectively. The fracture toughness of shale is often measured following the methods suggested by the International Society of Rock Mechanics (ISRM).[45−49] Based on the experimental results in the literature, G_c of shale is in the range of about 0.3−38 J/m^2.[45,46,50] The K_{Ic} of quartz, a component of inorganic matter in shale, is about 0.6−0.7 MPa·m$^{1/2}$ from micron-scale measurements and 0.8−0.9 MPa·m$^{1/2}$ by molecular simulations.[22,51,52] By assuming a Young's modulus of 72 GPa and a Poisson's ratio of 0.17,[51] G_c of quartz is about 5.5−10.8 J/m^2. Illite is one of the weak components of shale (G_c = 0.3−0.5 J/m^2, direction normal to the layer).[15,17] To examine the mechanical properties of illite, we perform molecular simulations for the tensile failure of illite in the directions perpendicular and parallel to the layers (see Figures S13 and S14). The results of G_c are about 0.5 and 5.2 J/m^2, respectively. The G_c of the kerogen matrix is lower than that of illite, even in the direction normal to the layer. In this regard, kerogen may be viewed as a weaker component than illite in shale. Our results reinforce the critical evidence that kerogen is potentially a mechanically weak component which may serve as the region for the fracture initiation and propagation in shale. Based on the results in Table 1, G_c is higher than $2\gamma_s$ in all types of kerogen. The difference is due to the plastic deformation during the tensile failure which is consistent with Irwin's theory.[10,13,14] Generally, the critical stress σ_c of a sample with a crack can be estimated based on the theories of Griffith and Irwin. However, one may overestimate the critical stress because of neglecting the effect of pores, for which a correction factor should be included. A discussion on this topic is presented in the Supporting Information.

4. CONCLUSIONS

The main conclusions drawn from this study are as follows:

(1) In a kerogen matrix, the stress−strain curves start with a linear behavior at small loadings, followed by plastic deformation and rupture.

(2) Kerogen type has a significant effect on tensile failure, which exhibits different modes. The high content of aliphatic carbons may lead to more ductile behavior and lower porosity, while a higher content of aromatic carbons may result in relatively higher brittleness and higher porosity.

(3) The fracture toughness of kerogen is lower than that of illite. Various evidence indicates that kerogen is potentially a mechanically weak component in shale, which may serve as a spot of fracture initiation and preferential fracture propagation path, especially in the highly decomposed region.

(4) In kerogen, the critical energy release rate G_c is 2 times higher than the surface energy density, $2\gamma_s$, which is an indication of pronounced plastic deformation during the tensile failure based on Irwin's theory.

Organic matters in shale rocks generally have complicated components, including kerogen, asphaltenes, resins, and light hydrocarbons. Kerogen molecules may also have different degrees of cross-linking. Fluids, including H_2O and CO_2, may invade into shale rocks during various processes. The overall properties may be affected by these factors significantly. These effects will be analyzed in our future work.

■ ASSOCIATED CONTENT

Supporting Information

The Supporting Information is available free of charge at https://pubs.acs.org/doi/10.1021/acs.jpcc.0c03158.

Size dependency analysis; mechanical property calculation; molecular simulations of tensile failure in illite; discussion about the estimation of critical stress in the kerogen matrix with crack; molecular structures of kerogen macromolecules; details of constructed kerogen matrices; radial distribution function of carbon atoms; pore size distribution of kerogen matrices; tensile failure process of different kerogen types; pore space evolution in the plastic region; and kerogen matrices for surface energy density calculation (PDF)

■ AUTHOR INFORMATION

Corresponding Author

Abbas Firoozabadi − *Reservoir Engineering Research Institute, Palo Alto, California 94301, United States; Chemical and Biomolecular Engineering Department, Rice University, Houston, Texas 70057, United States;* orcid.org/0000-0001-6102-9534; Email: af@rerinst.org

Author

Tianhao Wu − *Reservoir Engineering Research Institute, Palo Alto, California 94301, United States;* orcid.org/0000-0002-4749-6707

Complete contact information is available at: https://pubs.acs.org/10.1021/acs.jpcc.0c03158

Notes

The authors declare no competing financial interest.

■ ACKNOWLEDGMENTS

This work was supported by the member companies of the Reservoir Engineering Research Institute (RERI). Their support is appreciated.

■ REFERENCES

(1) US Energy Information Administration. Annual Energy Outlook 2019: With Projections to 2050. https://www.eia.gov/outlooks/aeo/ (accessed January 29, 2020).

(2) US Energy Information Administration. Technically Recoverable Shale Oil and Shale Gas Resources. https://www.eia.gov/analysis/studies/worldshalegas/ (accessed January 22, 2020).

(3) Middleton, R. S.; Carey, J. W.; Currier, R. P.; Hyman, J. D.; Kang, Q.; Karra, S.; Jiménez-Martínez, J.; Porter, M. L.; Viswanathan, H. S. Shale Gas and Non-Aqueous Fracturing Fluids: Opportunities and Challenges for Supercritical CO2. *Appl. Energy* **2015**, *147*, 500−509.

(4) Gandossi, L. An Overview of Hydraulic Fracturing and Other Formation Stimulation Technologies for Shale Gas Production. *European Commission Joint Research Centre Technical Reports*, 2013; p 26347.

(5) Liu, H.; Wang, F.; Zhang, J.; Meng, S.; Duan, Y. Fracturing with Carbon Dioxide: Application Status and Development Trend. *Pet. Explor. Dev.* **2014**, *41*, 513−519.
(6) Sinal, M. L.; Lancaster, G. Liquid CO2 Fracturing: Advantages and Limitations. *J. Can. Pet. Technol.* **1987**, *26*, 26−30.
(7) Wu, T.; Zhao, J.; Zhang, W.; Zhang, D. Nanopore Structure and Nanomechanical Properties of Organic-Rich Terrestrial Shale: An Insight into Technical Issues for Hydrocarbon Production. *Nano Energy* **2020**, *69*, 104426.
(8) Li, S.; Zhang, D. How Effective Is Carbon Dioxide as an Alternative Fracturing Fluid? *SPE J.* **2019**, *24*, 857−876.
(9) Anderson, T. L. *Fracture Mechanics: Fundamentals and Applications*; CRC Press: Boca Raton, 2005.
(10) Irwin, G. R. Analysis of Stresses and Strains near the End of a Crack Traversing a Plate. *J. Appl. Mech.* **1957**, *24*, 361−364.
(11) Griffith, A. A. The Phenomena of Rupture and Flow in Solids. *Philos. Trans. R. Soc. London, Ser. A* **1921**, *221*, 163−198.
(12) Griffith, A. A. The Theory of Rupture. *Proceedings of the First International Congress for Applied Mechanics*, 1924; pp 55−63.
(13) Irwin, G. R. Fracture Dynamics. *Fracturing of Metals*; ASM: Cleveland, 1948; pp 147−166.
(14) Irwin, G. R. Fracture. In *Elasticity and Plasticity/ Elastizität Und Plastizität*; Flügge, S., Ed.; Springer Berlin Heidelberg: Berlin, Heidelberg, 1958; pp 551−590.
(15) Hantal, G.; Brochard, L.; Laubie, H.; Ebrahimi, D.; Pellenq, R. J.-M.; Ulm, F.-J.; Coasne, B. Atomic-Scale Modelling of Elastic and Failure Properties of Clays. *Mol. Phys.* **2014**, *112*, 1294−1305.
(16) Brochard, L.; Hantal, G.; Laubie, H.; Ulm, F.-J.; Pellenq, R. J. M. Capturing Material Toughness by Molecular Simulation: Accounting for Large Yielding Effects and Limits. *Int. J. Fract.* **2015**, *194*, 149−167.
(17) Hantal, G.; Brochard, L.; Pellenq, R. J.-M.; Ulm, F.-J.; Coasne, B. Role of Interfaces in Elasticity and Failure of Clay−Organic Nanocomposites: Toughening Upon Interface Weakening? *Langmuir* **2017**, *33*, 11457−11466.
(18) Heider, Y.; Reiche, S.; Siebert, P.; Markert, B. Modeling of Hydraulic Fracturing Using a Porous-Media Phase-Field Approach with Reference to Experimental Data. *Eng. Fract. Mech.* **2018**, *202*, 116−134.
(19) Zhou, S.; Zhuang, X.; Rabczuk, T. Phase-Field Modeling of Fluid-Driven Dynamic Cracking in Porous Media. *Comput. Methods Appl. Mech. Eng.* **2019**, *350*, 169−198.
(20) Wu, T.; Li, X.; Zhao, J.; Zhang, D. Multiscale Pore Structure and Its Effect on Gas Transport in Organic-Rich Shale. *Water Resour. Res.* **2017**, *53*, 5438−5450.
(21) Patil, S. P.; Heider, Y.; Hernandez Padilla, C. A.; Cruz-Chú, E. R.; Markert, B. A Comparative Molecular Dynamics-Phase-Field Modeling Approach to Brittle Fracture. *Comput. Methods Appl. Mech. Eng.* **2016**, *312*, 117−129.
(22) Hantal, G.; Brochard, L.; Dias Soeiro Cordeiro, M. N.; Ulm, F. J.; Pellenq, R. J.-M. Surface Chemistry and Atomic-Scale Reconstruction of Kerogen−Silica Composites. *J. Phys. Chem. C* **2014**, *118*, 2429−2438.
(23) Bousige, C.; et al. Realistic Molecular Model of Kerogen's Nanostructure. *Nat. Mater.* **2016**, *15*, 576−582.
(24) Ungerer, P.; Collell, J.; Yiannourakou, M. Molecular Modeling of the Volumetric and Thermodynamic Properties of Kerogen: Influence of Organic Type and Maturity. *Energy Fuels* **2015**, *29*, 91−105.
(25) Wu, T.; Firoozabadi, A. Mechanical Properties and Failure Envelope of Kerogen Matrix by Molecular Dynamics Simulations. *J. Phys. Chem. C* **2020**, *124*, 2289−2294.
(26) Plimpton, S. Fast Parallel Algorithms for Short-Range Molecular Dynamics. *J. Comput. Phys.* **1995**, *117*, 1−19.
(27) Humphrey, W.; Dalke, A.; Schulten, K. VMD: Visual Molecular Dynamics. *J. Mol. Graph.* **1996**, *14*, 33−38.
(28) Collell, J.; Galliero, G.; Vermorel, R.; Ungerer, P.; Yiannourakou, M.; Montel, F.; Pujol, M. Transport of Multicomponent Hydrocarbon Mixtures in Shale Organic Matter by Molecular Simulations. *J. Phys. Chem. C* **2015**, *119*, 22587−22595.
(29) Tesson, S.; Firoozabadi, A. Methane Adsorption and Self-Diffusion in Shale Kerogen and Slit Nanopores by Molecular Simulations. *J. Phys. Chem. C* **2018**, *122*, 23528−23542.
(30) Ho, T. A.; Wang, Y.; Criscenti, L. J. Chemo-Mechanical Coupling in Kerogen Gas Adsorption/Desorption. *Phys. Chem. Chem. Phys.* **2018**, *20*, 12390−12395.
(31) Huang, L.; Ning, Z.; Wang, Q.; Zhang, W.; Cheng, Z.; Wu, X.; Qin, H. Effect of Organic Type and Moisture on CO2/CH4 Competitive Adsorption in Kerogen with Implications for CO2 Sequestration and Enhanced CH4 Recovery. *Appl. Energy* **2018**, *210*, 28−43.
(32) Obliger, A.; Ulm, F.-J.; Pellenq, R. Impact of Nanoporosity on Hydrocarbon Transport in Shales' Organic Matter. *Nano Lett.* **2018**, *18*, 832−837.
(33) Yiannourakou, M.; Ungerer, P.; Leblanc, B.; Rozanska, X.; Saxe, P.; Vidal-Gilbert, S.; Gouth, F.; Montel, F. Molecular Simulation of Adsorption in Microporous Materials. *Oil Gas Sci. Technol.* **2013**, *68*, 977−994.
(34) MedeA Version 3.0. https://www.materialsdesign.com/ (accessed May 2020).
(35) Hockney, R.; Eastwood, J. *Computer Simulation Using Particles*; Adam Hilger: New York, 1989; p 185.
(36) Waldman, M.; Hagler, A. T. New Combining Rules for Rare Gas van der Waals Parameters. *J. Comput. Chem.* **1993**, *14*, 1077−1084.
(37) Zhao, J.; Zhang, D.; Wu, T.; Tang, H.; Xuan, Q.; Jiang, Z.; Dai, C. Multiscale Approach for Mechanical Characterization of Organic-Rich Shale and Its Application. *Int. J. GeoMech.* **2019**, *19*, 04018180.
(38) Wilkinson, T. M.; Zargari, S.; Prasad, M.; Packard, C. E. Optimizing Nano-Dynamic Mechanical Analysis for High-Resolution, Elastic Modulus Mapping in Organic-Rich Shales. *J. Mater. Sci.* **2015**, *50*, 1041−1049.
(39) Goodarzi, M.; Rouainia, M.; Aplin, A. C.; Cubillas, P.; de Block, M. Predicting the Elastic Response of Organic-Rich Shale Using Nanoscale Measurements and Homogenisation Methods. *Geophys. Prospect.* **2017**, *65*, 1597−1614.
(40) Emmanuel, S.; Eliyahu, M.; Day-Stirrat, R. J.; Hofmann, R.; Macaulay, C. I. Impact of Thermal Maturation on Nano-Scale Elastic Properties of Organic Matter in Shales. *Mar. Pet. Geol.* **2016**, *70*, 175−184.
(41) Wang, Z.; Wang, H.; Cates, M. E. Effective Elastic Properties of Solid Clays. *Geophysics* **2001**, *66*, 428−440.
(42) Ahrens, T. J. *Mineral Physics & Crystallography: A Handbook of Physical Constants*; American Geophysical Union: Washington, DC, USA, 1995; Vol. 2.
(43) Wu, T.; Firoozabadi, A. Effect of Microstructural Flexibility on Methane Flow in Kerogen Matrix by Molecular Dynamics Simulations. *J. Phys. Chem. C* **2019**, *123*, 10874−10880.
(44) Düren, T.; Millange, F.; Férey, G.; Walton, K. S.; Snurr, R. Q. Calculating Geometric Surface Areas as a Characterization Tool for Metal−Organic Frameworks. *J. Phys. Chem. C* **2007**, *111*, 15350−15356.
(45) Chandler, M. R.; Meredith, P. G.; Brantut, N.; Crawford, B. R. Fracture Toughness Anisotropy in Shale. *J. Geophys. Res.: Solid Earth* **2016**, *121*, 1706−1729.
(46) Wang, H.; Zhao, F.; Huang, Z.; Yao, Y.; Yuan, G. Experimental Study of Mode-I Fracture Toughness for Layered Shale Based on Two ISRM-Suggested Methods. *Rock Mech. Rock Eng.* **2017**, *50*, 1933−1939.
(47) Kuruppu, M. D.; Obara, Y.; Ayatollahi, M. R.; Chong, K. P.; Funatsu, T. ISRM-Suggested Method for Determining the Mode I Static Fracture Toughness Using Semi-Circular Bend Specimen. *Rock Mech. Rock Eng.* **2014**, *47*, 267−274.
(48) Fowell, R.; Hudson, J.; Xu, C.; Zhao, X. Suggested Method for Determining Mode I Fracture Toughness Using Cracked Chevron Notched Brazilian Disc (CCNBD) Specimens. *Int. J. Rock Mech. Min. Sci. Geomech. Abstr.* **1995**, *32*, 57.

https://dx.doi.org/10.1021/acs.jpcc.0c03158
J. Phys. Chem. C 2020, 124, 15895−15901

(49) Franklin, J.; Zongqi, S.; Atkinson, B.; Meredith, P.; Rummel, F.; Mueller, W.; Nishimatsu, Y.; Takahahsi, H.; Costin, L.; Ingraffea, A. Suggested Methods for Determining the Fracture Toughness of Rock. *Int. J. Rock Mech. Min. Sci. Geomech. Abstr.* **1988**, *25*, 71.
(50) Mahanta, B.; Tripathy, A.; Vishal, V.; Singh, T. N.; Ranjith, P. G. Effects of Strain Rate on Fracture Toughness and Energy Release Rate of Gas Shales. *Eng. Geol.* **2017**, *218*, 39−49.
(51) Mueller, M. G.; Pejchal, V.; Žagar, G.; Singh, A.; Cantoni, M.; Mortensen, A. Fracture Toughness Testing of Nanocrystalline Alumina and Fused Quartz Using Chevron-Notched Microbeams. *Acta Mater.* **2015**, *86*, 385−395.
(52) Rimsza, J. M.; Jones, R. E.; Criscenti, L. J. Crack Propagation in Silica from Reactive Classical Molecular Dynamics Simulations. *J. Am. Ceram. Soc.* **2018**, *101*, 1488−1499.

https://dx.doi.org/10.1021/acs.jpcc.0c03158
J. Phys. Chem. C 2020, 124, 15895−15901